Bow shocks, bow waves, and dust waves. II. Beyond the rip point

William J. Henney & S. J. Arthur

Instituto de Radioastronomía y Astrofísica, Universidad Nacional Autónoma de México, Apartado Postal 3-72, 58090 Morelia, Michoacán, México

ABSTRACT

Dust waves are a result of gas–grain decoupling in a stream of dusty plasma that flows past a luminous star. The radiation field is sufficiently strong to overcome the collisional coupling between grains and gas at a *rip-point*, where the ratio of radiation pressure to gas pressure exceeds a critical value of roughly 1000. When the rip point occurs outside the hydrodynamic bow shock, a separate dust wave may form, decoupled from the gas shell, which can either be drag-confined or inertia-confined, depending on the stream density and relative velocity. In the drag-confined case, there is a minimum stream velocity of roughly $60\,\mathrm{km\,s^{-1}}$ that allows a steady-state stagnant drift solution for the dust wave apex. For lower relative velocities, the dust dynamics close to the axis exhibit a limit cycle behavior (rip and snap back) between two different radii. Strong coupling of charged grains to the plasma's magnetic field can modify these effects, but for a quasi-parallel field orientation the results are qualitatively similar to the non-magnetic case. For a quasi-perpendicular field, on the other hand, the formation of a decoupled dust wave is strongly suppressed.

Key words: circumstellar matter – radiation: dynamics – stars: winds, outflows

1 INTRODUCTION

In § 2 we calculate analytical models of the shape of dust waves in the drag-free limit. In §3 we discuss the relevant dust physics and the Cloudy models that we employ. In § 4 we calculate in detail the grain charging and dynamics, subject to radiation and drag forces, in order to determine the rip point where gas–grain coupling catastrophically breaks down. This is used to determine existence conditions for the presence of a decoupled dust wave. In § 5 we consider the additional coupling between the grains and the plasma's magnetic field, and how this effects the existence and structure of dust waves. In Appendix A we provide additional technical information on the numerical calculation of grain trajectories.

2 DUST WAVES IN THE DRAG-FREE LIMIT

In the optically thin limit, a spherical dust grain of radius a situated a distance R from a point source of radiation with luminosity spectrum L_ν will experience a repulsive, radially directed radiative force (e.g., Spitzer 1978)

$$f_\mathrm{rad} = \frac{\pi a^2}{4\pi R^2 c} \int_0^\infty Q_\mathrm{p}\, L_\nu\, d\nu \qquad (1)$$

where Q_p is the frequency-dependent radiation pressure efficiency[1] of the grain, and c is the speed of light.

---

[1] For absorption efficiency Q_abs, scattering efficiency Q_scat, and asymmetry parameter (mean scattering cosine) g, we have $Q_\mathrm{p} = Q_\mathrm{abs} + (1-g)Q_\mathrm{scat}$ (e.g., § 4.5 of Bohren & Huffman 1983).

If f_rad is the only force experienced by the grain, then it will move on a *ballistic* trajectory, determined by its initial speed at large distance, v_∞, and its impact parameter, b. For $b = 0$, the grain radially approaches the source with initial radial velocity $-v_\infty$, which is decelerated to zero at the distance of closest approach, R_{**}, given by energy conservation:

$$R_{**} = \frac{\kappa_\mathrm{d} L}{2\pi c v_\infty^2}\,, \qquad (2)$$

where we have defined a frequency-averaged single-grain opacity $(\mathrm{cm^2\,g^{-1}})$ as

$$\kappa_\mathrm{d} = \frac{\pi a^2}{m_\mathrm{d} L} \int_0^\infty Q_\mathrm{p}\, L_\nu\, d\nu\,, \qquad (3)$$

in which m_d is the grain mass and L is the bolometric source luminosity. The grain then turns round and recedes from the source along the same radius, reaching a velocity of $+v_\infty$ at large distance. Note that R_{**} as given by equation (2) is formally identical to Paper I's equation (6), but with the important difference that it is for a single grain considered in isolation, rather than a well-coupled dusty plasma. If

For $b > 0$, the problem is formally identical to that of Rutherford scattering, or (modulo a change of sign) planetary orbits. The method of solution (via introduction of a centrifugal potential term and reduction to a 1-dimensional problem) can be found in any classical mechanics text (e.g., Landau & Lifshitz 1976, § 14). The trajectory, $R_\mathrm{d}(\theta; b)$, is found to be hyperbolic, characterized by an eccentricity, $\varepsilon = \left(1 + 4b^2/R_{**}^2\right)^{1/2}$, and polar angle of closest approach, $\theta_\mathrm{m} = \cos^{-1}\varepsilon^{-1}$. The trajectory is symmetrical about θ_m
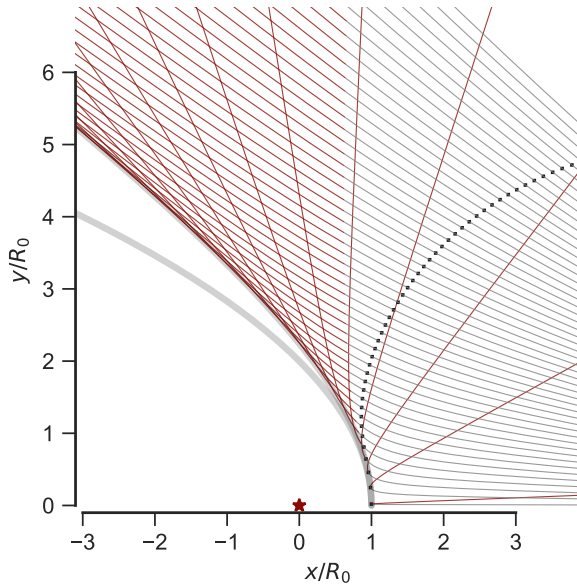
(a)
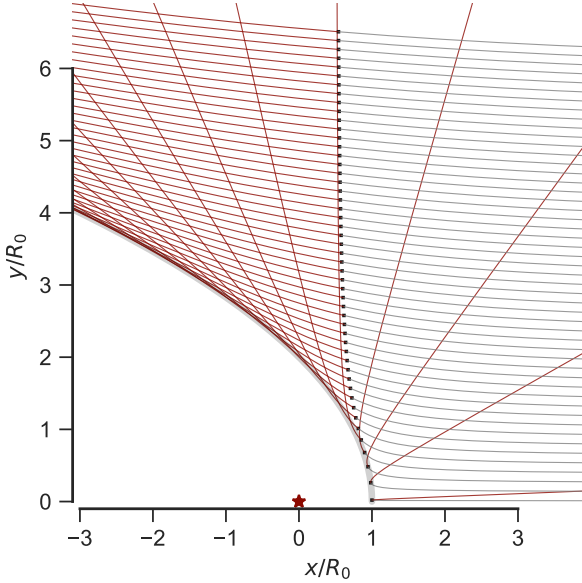
(b)

Figure 1. Dust grain trajectories under influence of a repulsive central r^{-2} radiative force. (a) A parallel stream of dust grains approach from the right at a uniform velocity and with a variety of impact parameters (initial y-coordinate). The central source is marked by a red star at the origin, and its radiative force deflects the trajectories into a hyperbolic shape, each of which reaches a minimum radius marked by a small black square. The incoming hyperbolic trajectories are traced in gray and the outgoing trajectories are traced in red. The locus of closest approach of the outgoing trajectories is parabolic in shape (traced by the thick, light gray line) and this constitutes the inner edge of the bow wave. (b) The same but for a divergent stream of dust grains that originates from a source on the x axis at a distance $D = 10R_{**}$ from the origin. In this case, the inner edge of the bow wave is hyperbolic and the parallel stream result is also shown for comparison.

and can be written as

$$\frac{R_{\mathrm{d}}(\theta; b)}{R_{**}} = \frac{\frac{1}{2}\left(\varepsilon^2 - 1\right)}{\varepsilon \cos(\theta - \theta_{\mathrm{m}}) - 1} , \qquad (4)$$

with a total deflection angle of $180° - 2\theta_{\mathrm{m}}$, which is equal to $90°$ when $b = 0.5R_{**}$.

2.1 Parallel dust stream

If the incoming dust grains initially travel along parallel trajectories with varying b, but the same v_∞, then deflection by the radiative force will form a bow-shaped dust wave around the radiation source, as shown in Figure 1. However, the inner edge of the dust wave, $R_{\mathrm{in}}(\theta)$ is not given by the closest approach along individual trajectories, $R_{\mathrm{d}}(\theta_{\mathrm{m}}; b)$, but instead must found by minimizing $R_{\mathrm{d}}(\theta; b)$ over all b for each value of θ, which yields

$$\frac{R_{\mathrm{in}}(\theta)}{R_{**}} = \frac{2}{1 + \cos\theta} . \qquad (5)$$

This is the polar form of the equation for the confocal parabola, which we have already discussed in detail in § 4 and Appendix C of Tarango-Yong & Henney (2018). Its planitude and alatude are $\Gamma = \Lambda = 2$ and these are unchanged under projection at any inclination.

2.2 Divergent dust stream

If the dust grains are assumed to originate from a second point source, located at a distance D from the radiation source, then the incoming stream will be divergent instead of plane parallel. The individual streamlines are not affected by this change and are still described by equation (4), except that the trajectory axes for $b > 0$ are no longer aligned with the global symmetry axis, so we must make the substitution $\theta \rightarrow \theta + \theta_1(b)$, where $\sin\theta_1 = b/D$ (see Fig. 3 of Tarango-Yong & Henney 2018). We parameterize the degree of divergence as $\mu = R_{**}/D$ and, as before, $R_{\mathrm{d}}(\theta + \theta_1(b, \mu); b)$ is minimized over all trajectories to find the shape of the bow wave's inner edge. This time, the result is a confocal hyperbola:

$$\frac{R_{\mathrm{in}}(\theta; \mu)}{R_{**}} = \frac{1 + \varepsilon_\mu}{1 + \varepsilon_\mu \cos\theta} , \qquad (6)$$

where the eccentricity is (to first order in μ) $\varepsilon_\mu = (1 - 2\mu)^{-1}$. An example is shown in Figure 1 for $\mu = 0.1$. Unsurprisingly, the resulting bow shape is more open than in the parallel stream case, increasingly so with increasing μ. The planitude and alatude are both equal: $\Pi = \Lambda = 1 + \varepsilon_\mu$.

2.3 Magnetized dust waves

We will show later in § 5 that for sufficiently small grains the Larmor magnetic gyration radius, r_{B} is typically small compared with other length scales of interest, and so the grains are effectively tied to the magnetic field lines. In this approximation, we can calculate the grain dynamics in the drag-free limit using f_{rad} as the sole force as above, but this time allowing acceleration only along the field lines. Assuming a uniform magnetic field, the only extra parameter needed is θ_{B}, the angle between the field direction and the direction of the dust stream (assumed to be plane parallel). The radiation force will also produce an out-of-plane drift, given by

$$\boldsymbol{v}_{\mathrm{drift}} = \frac{c}{ez_{\mathrm{d}}} \frac{f_{\mathrm{rad}} \times \boldsymbol{B}}{B^2} , \qquad (7)$$
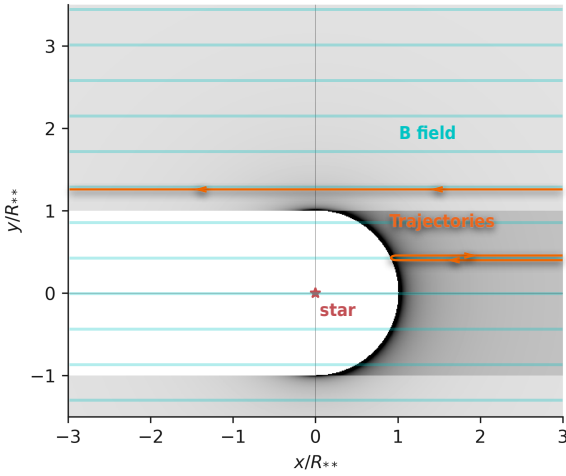
Figure 2. Dust wave formed by action of radiation forces on grains that are tightly coupled to a uniform parallel magnetic field. Two example trajectories, one with $b > R_{**}$ (upper) and one with $b < R_{**}$ (lower) are shown schematically in orange. The orientation of the magnetic field lines is shown in blue. The grayscale image shows the resultant dust density distribution.

but from equations (31, 1, 2) it follows that

$$\frac{v_{\text{drift}}(R_{**})}{v_\infty} = \frac{r_B}{2R_{**}} , \qquad (8)$$

so it is valid to ignore this drift in the limit of small r_B.

We now calculate in detail the grain trajectories in this limit for two cases, with the magnetic field oriented parallel and perpendicular to the stream[2] direction, respectively. These are sufficient to give a flavor of the effects of a magnetic field on the dust wave structure. Further models at intermediate angles, and which also include the effects of gas drag, are presented in § 5.

2.3.1 Parallel magnetic field

For $\theta_B = 0$, the $b = 0$ trajectory is identical to the non-magnetic case since the grain velocity and radiation force are both parallel to the field, which yields zero Lorentz force and zero $f \times B$ drift. Therefore, the axial turnaround radius, R_{**}, is still given by equation (2), whatever the value of r_B. For $b > 0$, f_{rad} has a component perpendicular to $\boldsymbol{B}$, which will induce a helical gyromotion around the field lines, but the guiding center must move parallel to the axis if $r_B \ll R_{**}$. Thus, the guiding center motion can be found from conservation of potential plus kinetic energy in one dimension:

$$\frac{v^2}{v_\infty^2} + V_{\text{rad}} = 1 , \qquad (9)$$

where V_{rad} is a suitably normalized potential of the projected radiation force along the field lines (x axis, where $x = R\cos\theta = b\cot\theta$):

$$V_{\text{rad}} = R_{**} \int_x^\infty \frac{\cos\theta}{R^2} \, dx = \frac{R_{**}\sin\theta}{b} = \frac{R_{**}}{R} . \qquad (10)$$

From equation (9), the trajectory must turn around when $V_{\text{rad}} = 1$, and equation (10) shows that this occurs at the same spherical radius,

$R = R_{**}$, for all impact parameters, b, so that the inner boundary of the dust wave is hemispherical in shape:

$$\frac{R_{\text{in}}(\theta)}{R_{**}} = 1 , \qquad (11)$$

yielding planitude and alatude of $\Pi = \Lambda = 1$. Note, however, that this only applies to streamlines with $b \leqslant R_{**}$. For those with $b > R_{**}$, the maximum V_{rad}, which occurs at $x = 0$, is smaller than unity, so that grains on these streamlines do not turn around, although they do slow down temporarily as they go past the star.

The grain density of the inflowing stream follows from mass continuity as:

$$n_d(R) = \frac{n\bar{m}Z_d}{m_d}\left(1 - \frac{R_{**}}{R}\right)^{-1/2} , \qquad (12)$$

where for simplicity we assume a single grain species of mass m_d and dust-gas ratio Z_d. The outflowing stream has exactly the same velocity profile as the inflowing one, apart from a change of sign for those streamlines that turn round. Therefore, in the region where the two streams co-exist ($y \leqslant R_{**}$, $x > 0$, and $R > R_{**}$), the total density is double that given by equation (12). This is illustrated in Figure 2.

2.3.2 Perpendicular magnetic field

For $\theta_B = 90°$, the guiding center is forced to move at a constant speed in the x direction, so that $x = -v_\infty t$, while the motion in the y direction obeys the ODE:

$$\frac{d^2 y}{dx^2} = \frac{1}{2}R_{**}\, y \left(x^2 + y^2\right)^{-3/2} . \qquad (13)$$

We have been unable to find an analytic solution to this equation, but a numerical solution is shown in Figure 3. When the impact parameter is larger than $b \sim R_{**}$, the trajectories are very similar to in the non-magnetic case (Fig. 1a). As shown in Figure 3b, the interaction of the grain with the radiation field in this large-b regime can be approximated as an impulsive acceleration of magnitude $\sim b^{-2}$ and duration $\sim b$, producing a final y velocity of $\sim b^{-1}$. Since the x velocity is constant, the total deflection angle is also of order $\sim b^{-1}$. The overlap of the outgoing trajectories produces a dense concentration of grains at the inner edge, which is roughly parabolic in shape. However, for $b < R_{**}$ the remorseless advance of the magnetic field does not allow the grains to slow down and turn round, as they do in the non-magnetic and parallel-field cases. As a result, no dense shell forms in the apex region, but instead there is a diffuse minimum in the density of grains around the star due to the high grain velocities reached there. This means that the apparent morphology of a pure dust wave becomes very sensitive to the radial dependence of the grain emissivity. If this is sufficiently steep, then the apex would coincide with the position of the star, although in practice the presence of a wind-supported bow shock, however small, will complicate the picture.

3 GRAIN CHARGING AND GAS–GRAIN COUPLING AROUND OB STARS

We calculate models of the physical properties of dust grains using the plasma physics code Cloudy (Ferland et al. 2013, 2017), which self-consistently solves the multi-frequency radiative transfer together with thermal, ionization, and excitation balance of all plasma constituents. Cloudy incorporates grain charging as described in
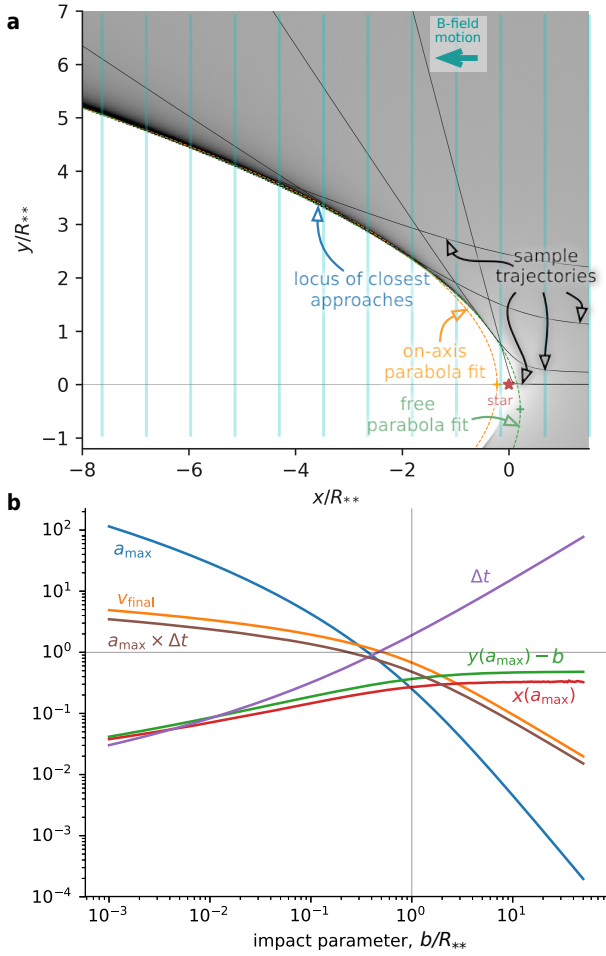
---

[2] In both cases, the stream trajectories are assumed parallel to one another, as in § 2.1.

Figure 3. Dust wave formed by action of radiation forces on grains that are tightly coupled to a uniform perpendicular magnetic field. (a) Sample trajectories are shown by thin black lines and the resultant dust density distribution in grayscale. Two parabolic fits to the inner edge of the dust wave in the wing region ($y > R_{**}$) are shown. The orange line shows a simultaneous fit to both wings, while the green line shows a fit to a single wing, in which the parabola apex is not constrained to lie on the axis. The second fit has much smaller residuals, indicating that the overall dust wave shape is "pointier" than a parabola, but this is hard to quantify because the disappearance of the dense shell in the apex region makes it impossible to define R_0 for the bow. (b) Trajectory parameters over a wide range of impact parameters, shown on a log–log scale. Distances are in units of R_{**}, times in units of R_{**}/v_∞, velocities in units of v_∞, and accelerations in units of v_∞^2/R_{**}. The grain's acceleration along the y axis has a maximum value, a_{max}, which occurs at a position $x(a_{max})$, $y(a_{max})$, just before the grain is swept past the star, with a duration (FWHM) of Δt. The grain's asymptotic y velocity is v_{final} and the fact that this closely tracks $a_{max} \times \Delta t$ indicates that the majority of the acceleration occurs in a sharp impulse. The curves tend to straight lines at the right side of the graph, which gives the asymptotic scaling relations discussed in the text.

Baldwin et al. (1991) and van Hoof et al. (2004) with photoelectric emission theory from Weingartner & Draine (2001a); Weingartner et al. (2006). We use the default "ISM" dust mixture included in Cloudy, which comprises ten size bins each for spherical silicate and graphite grains in the range 0.005 to 0.25 μm, and which is designed to reproduce the average Galactic extinction curve (Weingartner & Draine 2001b; Abel et al. 2008). The optical properties of each grain species are calculated using Mie theory (Bohren & Huffman
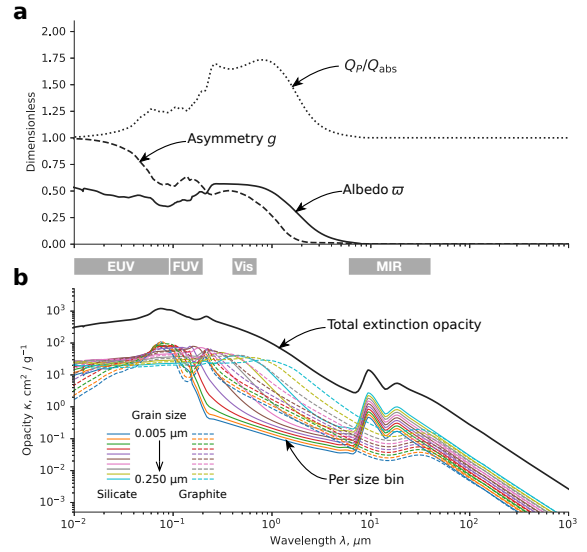

Figure 4. Extinction properties of Cloudy's standard "ISM" dust mixture. (a) Wavelength dependence of mean values over the entire mixture of three dimensionless quantities related to scattering: albedo, ϖ (solid line); scattering asymmetry, $g = \langle \cos\theta \rangle$ (dashed line); ratio of radiation pressure efficiency to absorption efficiency, Q_P/Q_{abs} (dotted line). (b) Wavelength dependence of mass opacity (cross section per unit mass of gas) for the whole mixture (heavy black line) and broken down by size bin and grain composition (colored lines, see key).

1983), assuming solid spheres. The resultant wavelength-dependent extinction properties of the mixture are summarised in Figure 4.

To ascertain the expected variation in grain properties in the circumstellar environs of luminous stars, we calculate a series of spherically symmetric, steady-state, constant density Cloudy simulations, illuminated by the stars listed in Table **??**, with stellar spectra taken from the OSTAR2002 and BSTAR2006 grids, calculated with the TLUSTY model atmosphere code (Lanz & Hubeny 2003, 2007). Simulations are run for hydrogen densities of 1, 10, 100, 10^3 and 10^4 cm^{-3} and assuming standard H II region gas phase abundances. The calculation is stopped when the ionization front is reached and the inner radius is chosen to be roughly 1% of this.

Figure 5 shows resultant radial profiles of dust properties for representative simulations: grain temperature, grain abundance, grain potential, and grain drift velocity. Line types correspond to the different size bins of graphite and silicate grains, as indicated in the key from smallest to largest. The left hand panels show results for a high-density ($n = 10^4$ cm^{-3}), compact ($R \approx 0.1$ pc) region around an early O star, where the grain temperature is very high, especially for the smaller silicate grains, and sublimation significantly reduces the grain abundance in the inner regions. The remaining columns show low-density ($n = 1$ cm^{-3}), extended ($R \sim 10$ pc) regions around main-sequence and supergiant B-type stars, in which the grain temperatures are much lower, ranging from 20 K to 50 K in the outer parts up to 100 K to 200 K in the inner parts.

Unlike the strong differences in thermal properties, the radial dependence of grain electrostatic potential (third row in Fig. 5) is qualitatively similar for all the simulations. The grains are predominantly positively charged, with high potentials (> 10 times the thermal energy of gas particles) close to the star due to the strong EUV and FUV photo-ejection. The potential falls to much lower
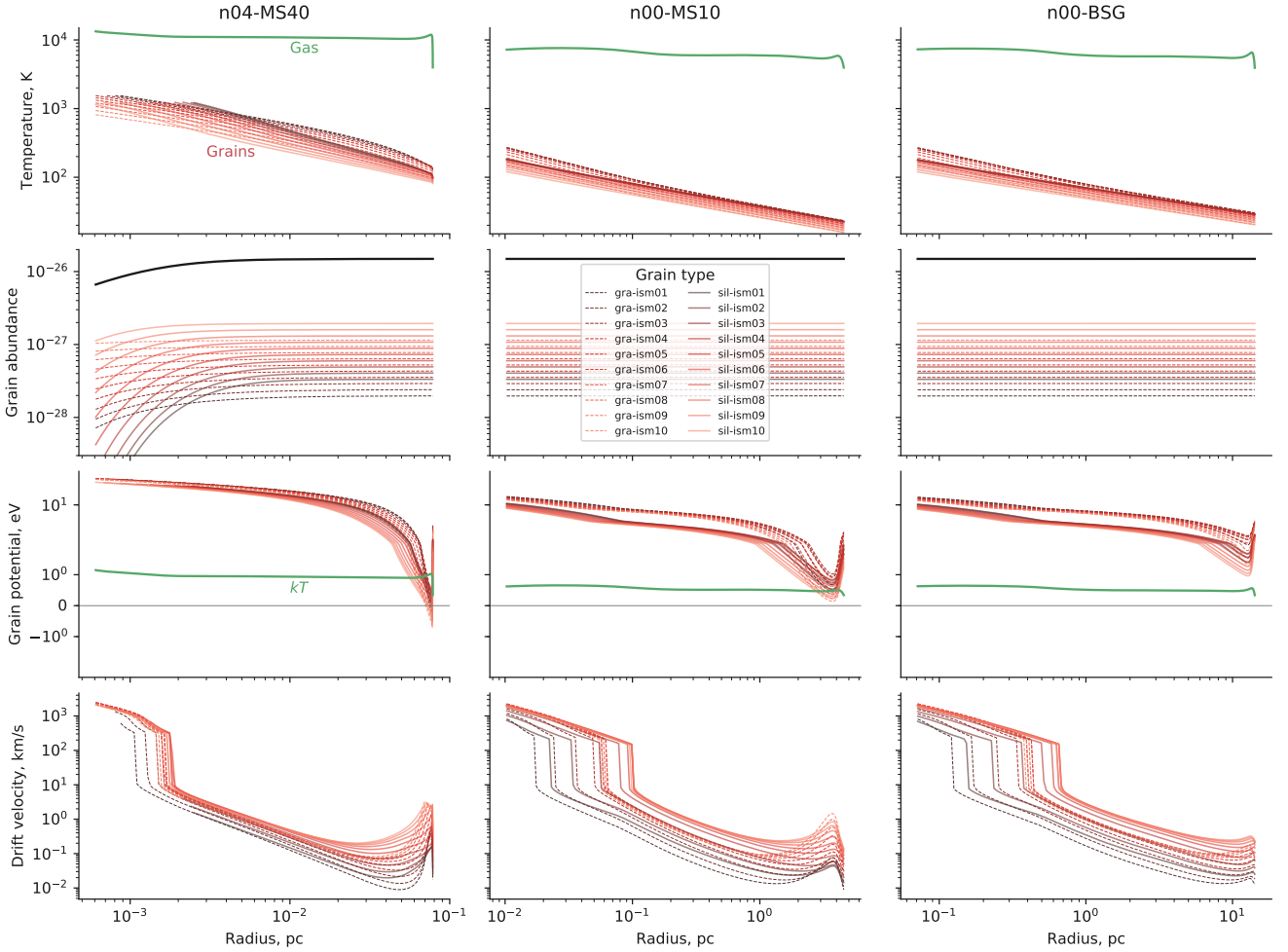
Figure 5. Dust properties as a function of radius from star for three selected Cloudy simulations. (a) $40\,M_\odot$ main-sequence star in medium of density $10^4\,cm^{-3}$. (b) $10\,M_\odot$ main-sequence star in medium of density $1\,cm^{-3}$. (c) Blue supergiant star in medium of density $1\,cm^{-3}$

.

values in the outer ionized region, as the EUV flux falls off, and then climbs again at the ionization front due to the fall in electron density, while the FUV photo-ejection persists well into the neutral region. There are small differences between the simulations due to the increasing relative importance of the EUV radiation for hotter stars, which leads to a deeper dip in the potential just inside the ionization front for the $40\,M_\odot$ case, even reaching negative values for some grain species.

Equilibrium drift velocity for each grain species is calculated in the Cloudy simulations using the same theory (Draine & Salpeter 1979) as outlined in § 4.1. The way that this is implemented by default in Cloudy means that if the only solution at the inner radius is a superthermal one, then the superthermal solution branch (upper right corner of Fig. 10) is followed as far as possible through the outer spatial zones. We have modified the code so as to instead always prefer the slower subthermal branch whenever multiple solutions are available. This makes the most sense in our context, where the grains are moving towards the star and so the radiative force is gradually increasing from an initial low value. Example results are shown in the bottom row of Figure 5 and again they are qualitatively similar for all the simulations. Close to the star, the radiation force is higher

than the upper limit on the Coulomb drag force (eq. [16]), so that the equilibrium drift velocity is exceedingly high.[3] As the radial distance from the star increases, the radiation field is increasingly diluted but the grain potential falls only slowly, so eventually one reaches a point where an equilibrium between Coulomb drag and radiation force can be established, which corresponds to a discontinuity in the drift velocity. This is the *rip point* discussed in § 4.2. The drift velocity carries on falling towards the outside of the H ii region, but then increases again just inside the ionization front due to the drop in grain potential there.

Both the charge balance and the force balance are essentially due to competition between the photons and the charged particles that interact with the grain. It is therefore reasonable to surmise that the gas–grain decoupling that occurs at the rip point might be determined principally by the ratio of photons to gas particles. We

---

[3] Note that such high drift velocities are much higher than any realistic true relative velocity between grains and gas, since they are based on the assumption that the radiation force remains constant while the grain is accelerated, which is not the case near the rip point. Instead, they are simply an indication that the gas and grains have completely decoupled.
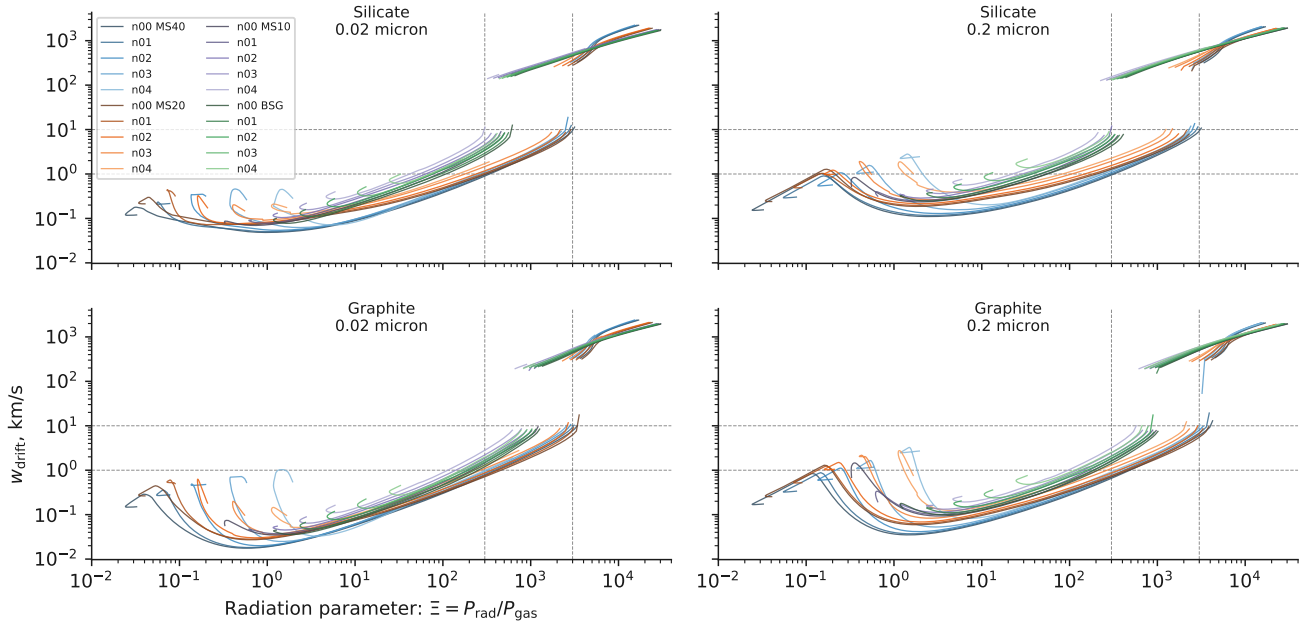
Figure 6. Drift velocity w_{drift} versus radiation parameter Ξ. Each line represents a simulation with ambient density and stellar type as indicated in the key. Results are shown for graphite and silicate grains of two different sizes. The rip point, which corresponds to gas–grain decoupling, is the discontinuity in the curves at $w_{\text{drift}} \approx 10\,\text{km}\,\text{s}^{-1}$, indicated by the upper horizontal dashed line. The vertical dashed lines show the narrow range of radiation parameter, $\Xi = 1000 \pm 0.5$ dex, that encompasses the rip point for all simulations.

test this hypothesis in Figure 6, where we characterize the photon-gas ratio by a dimensionless radiation parameter, Ξ, equal to the radiation pressure divided by the gas pressure. Results are shown for four different grain types and for all combinations of stellar parameters and ambient densities for which we have run simulations. It can be seen that the rip point does indeed always occur at a similar value of $\Xi \sim 1000$ for all simulations, albeit with some variation according to the spectral type of the star and the grain composition, as given in Table 2. The gas density and grain size have very little influence on this critical value $\Xi_{\dagger}$, with the only exception being the very smallest grains ($a < 0.006\,\mu\text{m}$, not illustrated), which show $\Xi_{\dagger} \approx 10^4$, but such grains are only minor contributors to the UV opacity ($< 10\%$ in EUV and $< 1\%$ in FUV, see Fig. 4).

Finally, Figure 7 shows the slow dependence of grain potential on radiation parameter for all the simulations on a linear versus logarithmic scale. The logarithmic fit of equation (19), most appropriate for carbon grains around cooler stars, is shown by the solid line. The dashed lines show the modifications for silicate grains and for hotter stars (see § 4.2). Further details of the Cloudy dust models are discussed in Appendix **??**.

Figure 7. Grain potential in thermal units (linear scale) versus radiation parameter (logarithmic scale). All densities and stellar types are shown, with line colors as in Fig. 6. Solid lines show silicate grains and dashed lines show graphite grains. Line width increases with grain size (to reduce clutter, only every second size bin is shown). The solid and dashed lines show the logarithmic fits discussed in the text.

4   IMPERFECT COUPLING BETWEEN GAS AND DUST

If the radiation field is sufficiently strong, then the collisional coupling between grains and gas will break down. In this section, we calculate the regions of star+stream parameter space where this might occur, leading to a separation of the bow into an outer dust wave and an inner, dust-free bow shock.

4.1   Drag force on grains

The drag force on a charged dust grain moving at a relative speed w through a plasma has contributions from both direct collisions and from electrostatic Coulomb interactions with ions and electrons. We use the expressions in Draine & Salpeter (1979), equations (4)–(6),
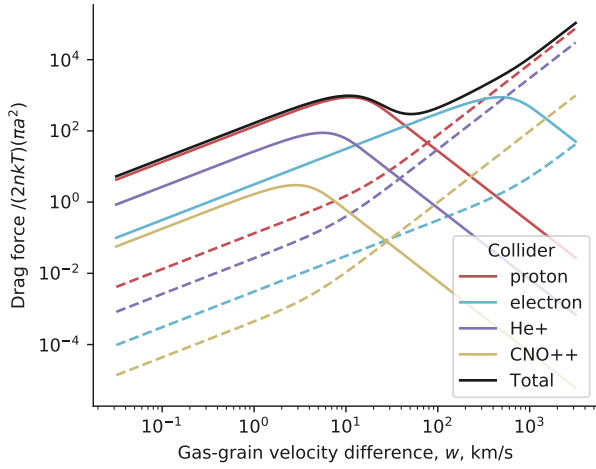
Figure 8. Contributions of different collider species to the dimensionless drag force, f_{drag}/f_*, as a function of gas–grain slip velocity, w. Solid lines show the Coulomb (electrostatic) drag, while dashed lines show the Epstein (solid-body) drag. Results are shown for dimensionless grain potential $\phi = 10$. All Coulomb forces scale with ϕ^2, while the Epstein forces are independent of ϕ. The species labelled "CNO++" represents the combined effect of all metals (see footnote 5).

Figure 9. Regimes of gas–grain drag as a function of slip velocity and grain potential. The different regimes are indicated by bold roman numerals, as explained in Table 1. Blue shading indicates regions dominated by Epstein (solid-body) drag, whereas red and green shading indicate regions dominated by Coulomb drag due to protons and electrons, respectively. In each case, the saturated color represents a contribution $> 70\%$ of the relevant component to the total drag force, while progressively lighter shading represents the $> 60\%$ and $> 50\%$ levels. The thick white dotted line indicates the transition between the subthermal and superthermal regimes for protons, while the thin white dotted line indicates the corresponding transition for electrons. Contours show the total drag force in units of f_* (see eq. [15]) in decade intervals from 0.1 to 10^4, as labelled. Results are shown for $T = 8000$ K and $n = 100$ cm^{-3}, but the differences are very slight throughout the ranges $T = 5000$ K to $15\,000$ K and $n = 10^{-3}$ cm^{-3} to 10^6 cm^{-3}.

Table 1. Regimes of drag force as function of grain potential and slip speed

	Regime	Approximate criteria	f_{drag}/f_*
I	Epstein subsonic	$\phi^2 \ll 1$ and $w_{10} < 1$	$1.5\, w_{10}$
II	Epstein supersonic	$w_{10} > 1$ and $w_{10} > 5\,|\phi|$	w_{10}^2
III	Coulomb p$^+$ subthermal	$\phi^2 > 1$ and $w_{10} < 1$	$(1 + 20\,\phi^2)\,w_{10}$
IV	Coulomb p$^+$ superthermal	$\phi^2 > 1$ and $1 < w_{10} < 5$	$w_{10}^2 + 10\,\phi^2/w_{10}^2$
V	Coulomb e$^-$ subthermal	$\phi^2 > 20$ and $5 < w_{10} < 42$	$0.48\,\phi^2\, w_{10}$

considering the contributions from protons, electrons, helium ions,[4] and metal ions.[5] Results are shown in Figure 8, where dashed lines correspond to direct solid body collisions and solid lines to electrostatic interactions. The latter depend on the grain potential, which is described in dimensionless terms by ϕ, which is the electrostatic potential energy of a unit charge at the surface of a grain of charge z_{d} and radius a, in units of the characteristic thermal energy of a gas particle:

$$\phi = \frac{e^2 z_{\mathrm{d}}}{akT} \, . \tag{14}$$

The electrostatic contributions to f_{drag} are proportional to ϕ^2 (results are shown for $|\phi| = 10$), whereas the solid-body contributions are independent of ϕ. The drag force is put in dimensionless units by

dividing by a characteristic force:

$$f_* = 2nkT \cdot \pi a^2 \, , \tag{15}$$

which is approximately[6] the ionized gas pressure multiplied by the grain geometric cross section.

For grains with low electric charge, $\phi^2 \ll 1$, the drag force is dominated by direct collisions of protons with the grain (dashed red line in Fig. 8). The gas collisional mean free path is much larger than the grain size, so the drag is in the Epstein regime (Weidenschilling 1977). As the relative gas–grain slip speed, w, increases, f_{drag} first increases linearly with w reaching $f_{\mathrm{drag}} \approx f_*$ at $w = c_{\mathrm{s}} \approx 10$ km s^{-1}, then transitions to a quadratic increase in the supersonic regime.

As $|\phi|$ increases, long-range electrostatic interactions with protons within the Debye radius (Coulomb drag) become increasingly important at subsonic relative velocities, as shown by the solid lines in Figure 8). However, the Coulomb drag has a peak when w is

---

[4] Helium is assumed to be singly ionized, leading to only a small contribution to the drag force. For much hotter stars, such as the central stars of planetary nebulae, helium may be doubly ionized, which leads to a fourfold increase in its Coulomb drag contribution, which is significant for $w < 5$ km s^{-1}.

[5] All metals are lumped together as a single species, assuming standard H II region gas-phase abundances. They are dominated by C and O, with minor contributions from N and Ne. The total abundance is 8.5×10^{-4} and the effective atomic weight is 15.3. All are assumed to be doubly ionized. Their largest relative contribution to the drag force is for $w < 2$ km s^{-1}, but is less than 1% even there.

[6] To simplify the exposition, the gas pressure in this section is calculated assuming a fully ionized, pure hydrogen plasma, yielding $P_{\mathrm{gas}} = 2nkT$. For typical ISM abundances, the contribution of helium and its corresponding electrons yield a correction to this of order 5%. The required modifications when a cool star interacts with a predominantly neutral gas stream are discussed later.
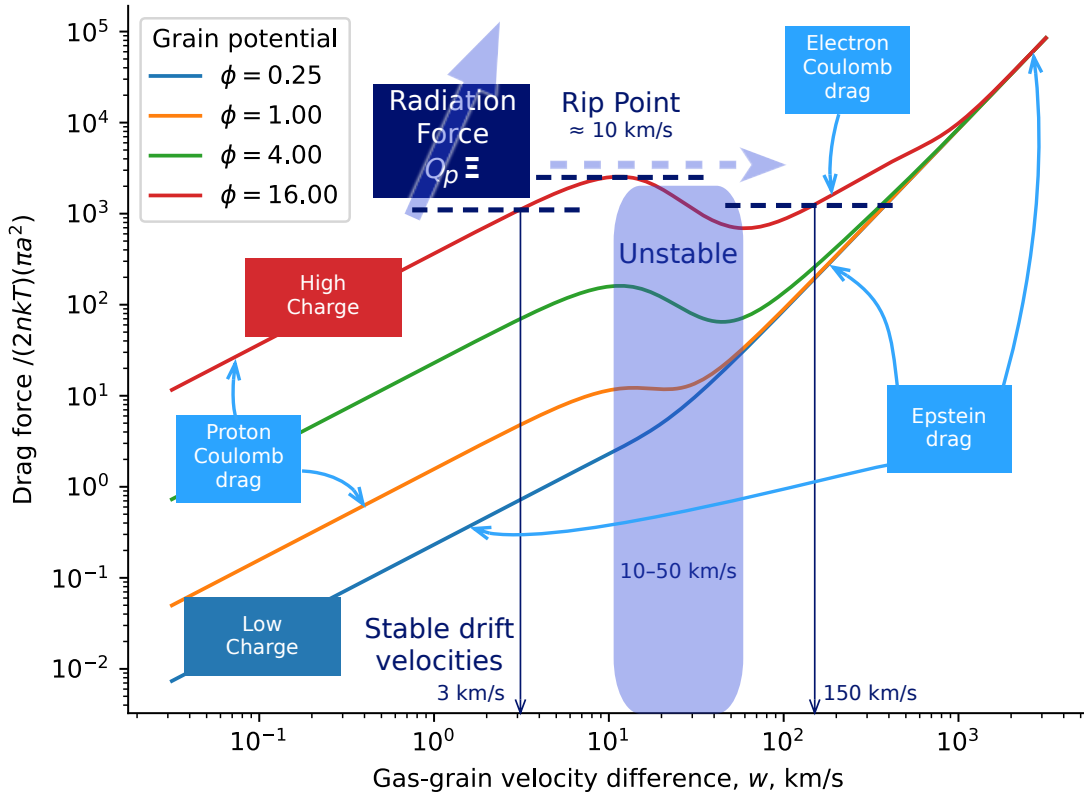
Figure 10. Dimensionless drag force, f_{drag}/f_*, as a function of gas–grain slip velocity, w, for different values of the grain potential in thermal units, ϕ. Contributions from proton and electron Coulomb (electrostatic) drag, as well as Epstein (solid-body) drag are indicated. Examples of subsonic and highly supersonic stable drift velocities are shown (thin dark blue arrows), where the drag force is in equilibrium with the radiation force (thick dark blue dashed lines), while blue shading indicates the unstable, mildly supersonic velocity regime, where no stable drift equilibrium exists. Inset graph shows ϕ as a function of the radiation parameter, $\Xi = P_{\mathrm{rad}}/P_{\mathrm{gas}}$ on a log–linear scale for a collection of Cloudy models (see Appendix 3).

equal to the thermal speed of the colliders, which is $\approx 10\,\mathrm{km\,s^{-1}}$ for protons, giving a maximum strength of

$$f_{\mathrm{max}} = 0.5\,(\ln\Lambda)\,\phi^2 f_* \approx 10\,\phi^2 f_* \,, \qquad (16)$$

where Λ is the plasma parameter (number of particles within a Debye volume), such that $\ln\Lambda = 23.267 + 1.5\ln T_4 - 0.5\ln n$. At highly super-thermal speeds, the Coulomb drag falls asymptotically as $f_{\mathrm{drag}} \propto 1/w^2$. The thermal speed of electrons is higher than that of the protons by a factor of $(m_p/m_e)^{1/2}$, so that the electron Coulomb drag (solid light blue line) gives a second peak of similar strength, but at $w \approx 430\,\mathrm{km\,s^{-1}}$. The behavior of f_{drag} in all these different regimes is summarised in Table 1, in terms of ϕ and $w_{10} = w/10\,\mathrm{km\,s^{-1}}$. This is further illustrated in Figure 9, where each of the drag regimes is located on the $(w,|\phi|)$ plane.

4.2 Gas–grain separation: drift and rip

In Appendix 2 we calculate the behaviour of an incoming stream of dust grains, subject only to the repulsive radiation force from a star. For an initial inward radial trajectory, the dust grain motion is decelerated and turned around, reaching a minimum radius R_{**}, given by equation (2). This drag-free radiative turnaround radius,

R_{**}, is smaller for higher initial inward velocities, but is independent of the density of the incoming stream. We are now in a position to see how gas–grain drag will modify this picture.

From equations (1) and (15), we can write the radiation force acting on a grain as

$$f_{\mathrm{rad}} = Q_{\mathrm{p}}\,\Xi\,f_* \,, \qquad (17)$$

where Q_{p} is the grain's radiation pressure efficiency (see footnote 1 in Appendix 2) and Ξ is the local radiation parameter, defined as the ratio of direct stellar radiation pressure to gas pressure:

$$\Xi \equiv \frac{P_{\mathrm{rad}}}{P_{\mathrm{gas}}} \approx \frac{L}{4\pi R^2 c\,(2nkT)} \,, \qquad (18)$$

where the last expression corresponds to the optically thin limit. The grain potential ϕ is also primarily determined by Ξ, as shown in Appendix 3 and the inset graph of Figure 10, but with a slow dependence, which can be approximated as

$$\phi(\Xi) \approx 1.5\,(2.3 + \ln\Xi) \,. \qquad (19)$$

There are also slight secondary dependencies on the grain composition and stellar spectrum. The relationship given in eq. (19) is appropriate for graphite grains and for stellar effective temperatures in the range $20\,\mathrm{kK}$ to $30\,\mathrm{kK}$. For hotter stars than this, ϕ should

Table 2. Critical values of radiation parameter at the rip point: $\Xi_\dagger$

Spectrum	Grain composition	
	Graphite	Silicate
B star	1000 ± 400	350 ± 150
O star	3000 ± 500	2500 ± 500

Calculated from the Cloudy models shown in Figure 6. Uncertainties represent variations with grain size and gas density. See Appendix 3 for further details.

be multiplied by a further factor of 1.5, while for silicate grains it should be divided by 1.5.

In the outer regions of the photoionized volume around an OB star, close to the ionization front, the radiation parameter is low, with typical value $\Xi \sim 0.1$. In this regime, the negative charge current at the grain surface due to electron collisions is roughly in balance with the positive current due to the ultraviolet photoelectric effect (Weingartner & Draine 2001a), leading to a low grain potential, $|\phi| < 1$, which may be positive or negative. The low Ξ means that the radiative force is also weak: $f_{\rm rad} \sim 0.1 f_*$ from equation (17) if $Q_{\rm p} \sim 1$ at UV wavelengths, which is true for all but the smallest grains. Thus, from the equations for $f_{\rm drag}$ given in Table 1, the radiative force can be balanced by Epstein drag if $w_{10} \sim 0.1$, leading to a small equilibrium drift velocity, $w_{\rm drift} < 1\,{\rm km\,s}^{-1}$, of the grains with respect to the gas. This drift is much smaller than the inward stream velocities that we are considering ($v_\infty > 10\,{\rm km\,s}^{-1}$), so the dust follows the gas stream at a slightly reduced velocity ($< 10\%$), and (by mass conservation) a slightly increased density. Each grain exerts an exactly opposite force to $f_{\rm drag}$ upon the gas, but since the dust-gas mass ratio, $Z_{\rm d}$, is small, this produces a negligible acceleration of the gas.

As the dusty stream approaches the star, the radiation parameter Ξ will increase, with a dependence of R^{-2} once the stream is well inside the ionization front. This increases $f_{\rm rad}$ (eq. [17]), but also increases the grain potential, ϕ (eq. [19]) due to the increasing dominance of grain charging by photoelectric ejection. Initially, this results in a lowering of the equilibrium drift velocity to $w_{10} \sim 0.01$ as the Coulomb drag kicks in (see Appendix 3). However, at smaller radii the slow logarithmic increase in $\phi(\Xi)$ means that the drift velocity must start increasing again to accommodate the linear increase of $f_{\rm rad}(\Xi)$. Eventually, $f_{\rm rad}$ exceeds $f_{\rm max}$, the maximum drag force that proton Coulomb interactions can provide (eq. [16]). This occurs at a critical value of the radiation parameter, which we denote the *rip point*: $\Xi_\dagger \sim 1000$. The variations in $\Xi_\dagger$ with star and grain parameters, which are of order ± 0.5 dex, are listed in Table 2 and illustrated graphically in Figure 6. The radius of the rip point, $R_\dagger$, can be expressed in terms of R_*, the fiducial optically thick bow shock radius introduced in Paper I's § 2.1:

$$R_\dagger = \frac{v_\infty}{c_{\rm s}} \Xi_\dagger^{-1/2} R_* \approx v_{10}\, \Xi_\dagger^{-1/2} R_* \,, \tag{20}$$

where we have made use of equation (18) and Paper I's equation (3).

What happens to the dust grain following this catastrophic breakdown of gas-grain coupling depends on the relation between the rip point radius, $R_\dagger$, and the drag-free radiative turnaround radius, R_{**}. If $R_\dagger > R_{**}$, then the grain's inertia will still carry it in as far as R_{**} and the initial trajectory will be almost identical to that described in Appendix 2 for the drag-free case. However, after being turned around by the radiation field and pushed out past $R_\dagger$ again, the grain will *recouple* to the gas and be dragged back for a

second approach.[7] We will refer to this as an *inertia-confined dust wave* (IDW). From equations (20, 22, 24), the condition $R_\dagger > R_{**}$ corresponds to $\tau_* < (\kappa/\kappa_{\rm d})\tau_{*,\rm max}$, which is indicated by dashed lines in the left panel of Figure 11. If, on the other hand, $R_\dagger < R_{**}$, then the tail wind provided by the gas carries the grain closer to the star than its inertia would naturally take it. When the grain finally decouples at $R_\dagger$ it experiences a much higher unbalanced $f_{\rm rad}$, which can initially accelerate it to outward velocities significantly higher than the inflow velocity if $R_\dagger \ll R_{**}$. We will refer to this case as a *drag-confined dust wave* (DDW).

4.3 Existence conditions for dust waves

In order for a separate outer dust wave to exist, it is necessary for the grains to decouple from the incoming gas stream before the stream hits the hydrodynamic bow shock caused by the stellar wind. The wind bow shock radius is $R_0 = \eta_{\rm w}^{1/2} R_*$ (Paper I's eq. [12]), where $\eta_{\rm w}$ is the wind momentum efficiency (Paper I's eq. [13]). Therefore, the condition $R_\dagger > R_0$ becomes from equation (20):

$$v_{10} > v_{10,\rm min} = \left(\Xi_\dagger\, \eta_{\rm w}\right)^{1/2} \,. \tag{21}$$

For early O main-sequence stars and OB supergiants, the wind efficiency is generally high ($\eta_{\rm w} > 0.1$) and $\Xi_\dagger > 2000$ (Tab. 2), so that dust waves can only exist when the stream velocity is very high ($v_\infty > 150\,{\rm km\,s}^{-1}$). For main-sequence B stars, in contrast, the wind can be much weaker ($\eta_{\rm w} < 0.01$) and $\Xi_\dagger$ is also smaller, so that dust waves are permitted by this criterion for much lower stream velocities: ($v_\infty > 30\,{\rm km\,s}^{-1}$). The same will be true of the "weak-wind" class of late O main-sequence stars, which also show $\eta_{\rm w} < 0.01$ (see Paper I, § 4).

However, there are other conditions that need to be satisfied in order for the dust wave to exist. For instance, the drag-free turnaround radius must also be outside the bow shock: $R_{**} > R_0$, otherwise the radiation is incapable of repelling the grain opportunely, even once it has decoupled from the gas. From equation (2), together with Paper I's equations (3, 9), we find

$$\frac{R_{**}}{R_*} = \frac{2\kappa_{\rm d}\tau_*}{\kappa} \,, \tag{22}$$

so the condition becomes

$$\tau_* > \tau_{*,\rm min} = 0.5\, \frac{\kappa}{\kappa_{\rm d}}\, \eta_{\rm w}^{1/2} \,. \tag{23}$$

The average value of the factor $\kappa/\kappa_{\rm d}$ over the entire grain population must be equal to the dust-gas mass ratio, $Z_{\rm d} \approx 0.01$, but the factor will vary between grains, according to their size and composition.[8] In particular, it will be relatively larger for the largest grains ($a \approx 0.2\,\mu{\rm m}$), which dominate the total dust mass, and smaller for the smaller grains ($a \approx 0.02\,\mu{\rm m}$), which dominate the UV opacity. Given the dependence of τ_* on the stream parameters (Paper I's eq. [15]), for a given stellar luminosity this condition corresponds to a minimum value for n/v_∞^2.

A third condition comes from requiring $R_\dagger > R_0$ in the radiation

---

[7] If the initial impact parameter of the trajectory is not strictly $b = 0$, then the resultant lateral component of $f_{\rm rad}$ will mean that b will be much increased for the second approach.

[8] Remember that κ is the opacity per unit mass of gas, while $\kappa_{\rm d}$ is the opacity per unit mass of a particular grain. In both cases, averaged over the stellar spectrum.
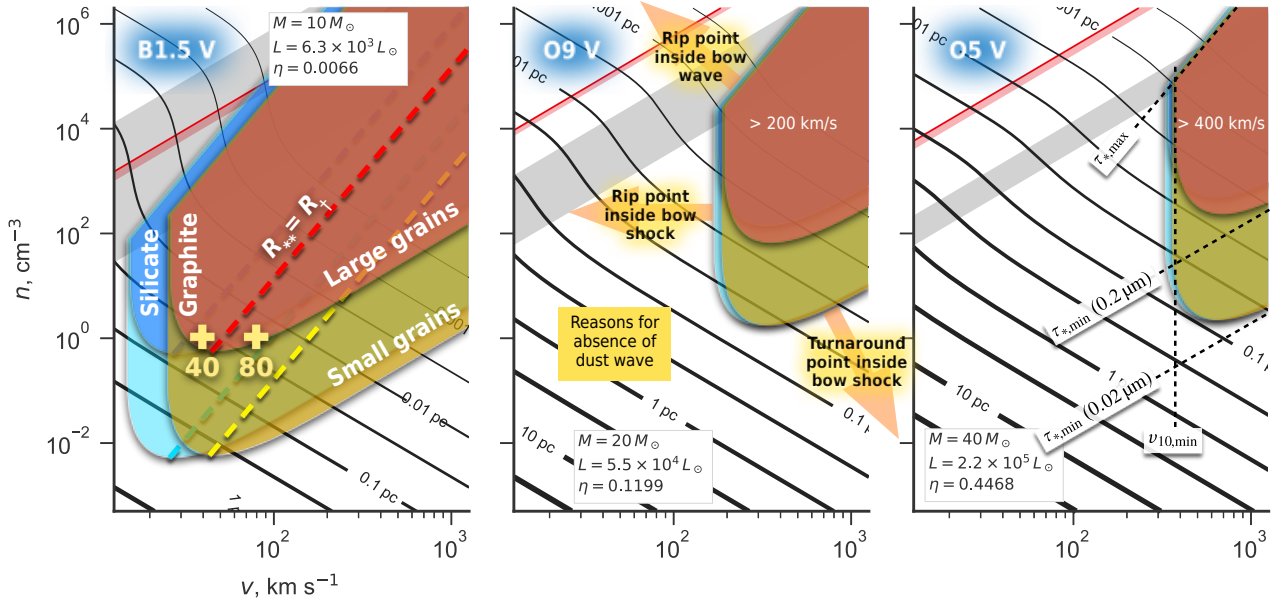
Figure 11. Regions of stream parameter space (v, n) where dust waves may form around main-sequence OB stars of $10\,M_\odot$, $20\,M_\odot$ and $40\,M_\odot$ (see Paper I's Tab. 1). This figure is similar to Paper I's Fig. 2, except that the velocity axis is logarithmic and extends out to $1000\,\mathrm{km\,s^{-1}}$. Overlapping colored shapes show parameters where dust waves may be allowed in the cases of large ($a = 0.2\,\mu\mathrm{m}$) and small ($a = 0.02\,\mu\mathrm{m}$) graphite and silicate grains, as labeled in the left panel. For (v, n) outside of these shapes, dust waves cannot occur for the reasons indicated by labeled orange arrows in the center panel. Labeled dashed lines in the right panel show the correspondence between the region boundaries and each dust wave existence condition given in equations (21, 23, 24). Heavy dashed lines in the left panel show where the rip point and the drag-free turnaround radius coincide. Dust waves above these lines are drag confined, while dust waves below the lines are inertia confined.

bow wave regime (see Paper I's § 2.1), where $R_0 \approx 2\tau_* R_*$. This yields

$$\tau_* < \tau_{*,\mathrm{max}} = 0.5\, v_{10}\, \Xi_\dagger^{-1/2}\,, \tag{24}$$

which, for a given stellar luminosity, corresponds to a maximum value for n/v_∞^4. Thus, for a given stream velocity that satisfies equation (21), equations (23, 24) determine respectively the minimum and maximum stream density for which a dust wave can exist.

The combined effects of the three conditions are illustrated in Figure 11 for each of the three example main sequence stars from Paper I's Table 1. Further restrictions on the existence of dust waves arise when the effects of magnetic fields are considered, as will be discussed in § 5 below. Note that the three conditions are restrictions solely on the formation of an *outer* dust wave, that is, outside of the wind-supported hydrodynamic bow shock. In the case of the equation (23) condition, there is a further possibility: if the gas–grain coupling (and magnetic coupling) is so weak that it is still unimportant at the higher densities found in the bow shock shell, then an inertia-confined *inner* dust wave may form inside the bow shock, even when $\tau_* < \tau_{*,\mathrm{min}}$. Although the same might be thought to apply to the condition of equation (21), this is not the case, since the density compression in the bow shock will reduce the radiation parameter, Ξ, which moves the rip point, $R_\dagger$, to an even smaller radius. Therefore, if radiation has not managed to decouple a grain before it passes through the shock, it is unlikely to be able to do it afterwards.

4.4 Grain trajectories along the symmetry axis

The post-decoupling behavior of the grain depends on the sign of df_{drag}/dw when $w = |v_\infty|$. If this derivative is positive, as is the case in drag regimes II and V (see Tab. 1 and Fig. 9), then the grain can reach a stable equilibrium drift at rest with respect to the star[9] at a point $R_\ddagger$, which we call the *stagnant drift radius*. If the stream velocity is not excessively high ($v_\infty < 150\,\mathrm{km\,s^{-1}}$ when $\phi = 4$, or $< 300\,\mathrm{km\,s^{-1}}$ when $\phi = 16$), then the equilibrium f_{rad} is less than the value at the rip point, requiring a lower value of the radiation parameter: $\Xi_\ddagger < \Xi_\dagger$. The resultant stagnant drift radius is therefore outside the rip point: $R_\ddagger > R_\dagger$.

On the other hand, if $df_{\mathrm{drag}}/dw < 0$ when $w = |v_\infty|$, then the equilibrium is unstable and no stagnant drift is possible. This occurs for drag regime IV, which applies when $\phi > 1$ and $10\,\mathrm{km\,s^{-1}} < v_\infty < 50\,\mathrm{km\,s^{-1}}$. There is also a second unstable regime (partially visible in the upper-right corner of Fig. 9), which is related to the thermal peak in the electron Coulomb drag when $\phi > 30$ and $400\,\mathrm{km\,s^{-1}} < v_\infty < 2000\,\mathrm{km\,s^{-1}}$, but this is not relevant to bow shocks around OB stars.[10]

An example of each of these two behaviors is illustrated in Figure 12. The left panels show the case where $v_\infty = 40\,\mathrm{km\,s^{-1}}$, which is in the unstable regime, resulting in periodic "limit-cycle"

---

[9] Again, this is only strictly true when the impact parameter is zero. However, as we show below, it is a reasonable approximation over a range of impact parameters in the case where the angle between the magnetic field direction and the stream velocity is not too large.

[10] It may apply in other contexts, such as outflows from AGN, since detailed modeling of grain charging around quasars (Weingartner et al. 2006) implies that grain potentials as high as $\phi \sim 100$ can be achieved.
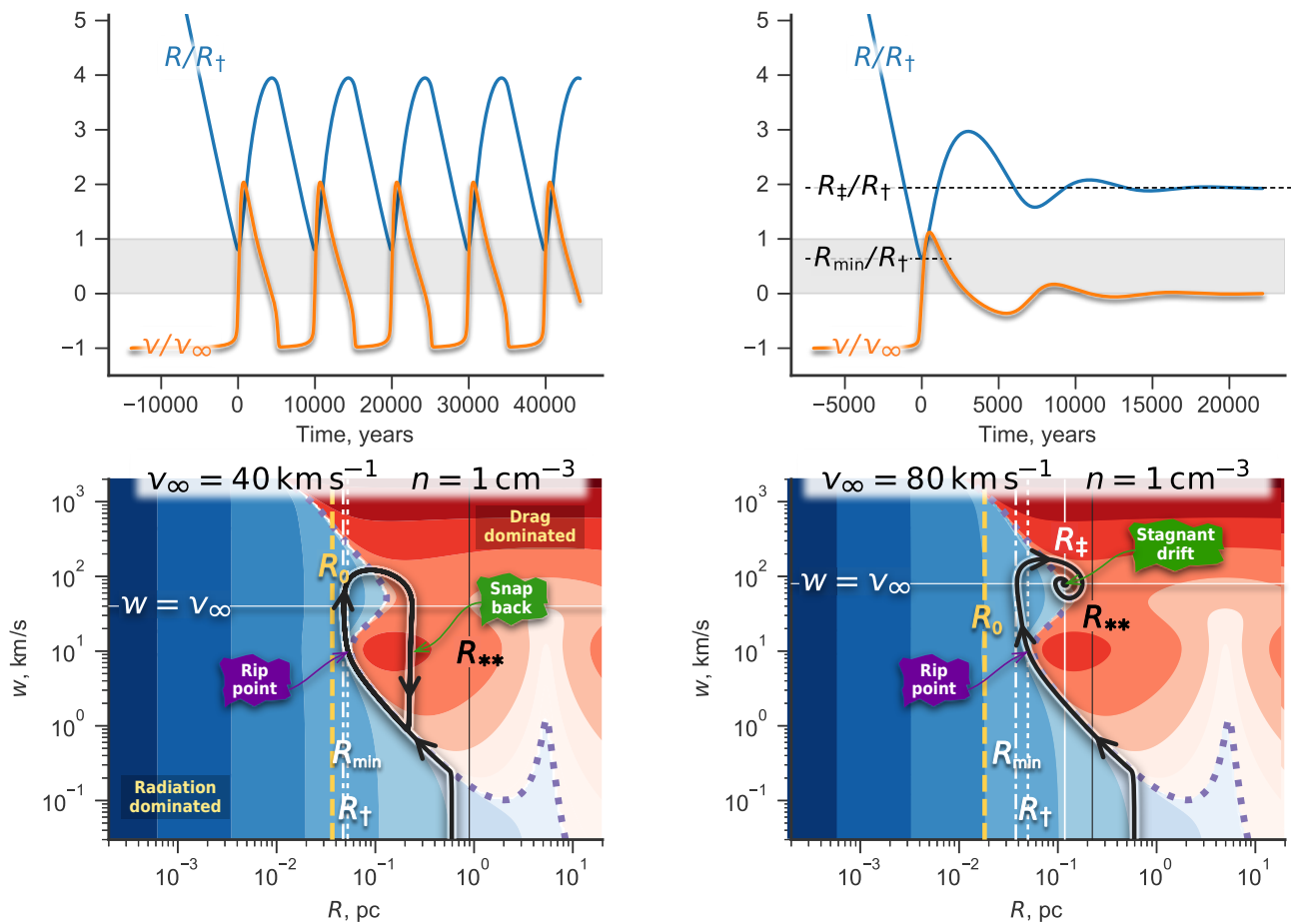
Figure 12. Trajectories of small graphite grains ($a = 0.02\,\mu\text{m}$) at impact parameter $b = 0$ for two example cases (see yellow "+" symbols in left panel of Fig. 11), which differ only in the stream velocity: $v = 40\,\text{km s}^{-1}$ (left panels) and $80\,\text{km s}^{-1}$ (right panels). In both cases, the stream density is $n = 1\,\text{cm}^{-3}$ and the central star is a $10\,\text{M}_\odot$ main-sequence B star (see Tab. **??**). Upper panels show the evolution of grain radius, R (blue curve, normalized by the rip point radius, $R_\dagger$), and grain velocity, v (orange curve, normalized by the gas stream velocity). The origin of the time axis is set to the moment of closest approach of the grain to the star: $R = R_{\text{min}}$. Lower panels show the trajectories in phase space: position versus gas–grain relative slip velocity ($w = |v - v_\infty|$). Filled contours show the net force on the grain: $f_{\text{rad}} - f_{\text{drag}}$, with positive values in blue and negative values in red. The heavy dotted line shows where there is no net force: $f_{\text{rad}} = f_{\text{drag}}$. The grain trajectory (thick, solid black line with arrows) initially follows this line, but departs from it after the rip point. In the left panel, the grain enters a limit cycle between decoupling (rip) and re-coupling (snap back). In the right panel, the grain spirals in on the stagnant drift point. See text for further details.

behavior (the parameters of this model correspond to the yellow "plus" symbol labeled "40" in the left panel of Fig. 11). During the grain's first approach, it starts to follow a phase trajectory (lower left panel) along the $f_{\text{rad}} - f_{\text{drag}} = 0$ contour, corresponding to equilibrium drift, in which the grain begins to move a few km s^{-1} slower than the gas stream. Then, when it reaches the rip point ($R = R_\dagger$, $w \approx 10\,\text{km s}^{-1}$) it suddenly experiences a large unbalanced outward radiation force (blue region of phase space in Fig. 12). The grain's inward momentum carries it to the point $R_{\text{min}} \approx 0.85R_\dagger$, before it is expelled at roughly twice the inflow speed. However, after moving outward, it finds itself in a drag-dominated region of phase space (red in the figure), and so recouples to the inflowing gas stream. The recoupling initiates gradually, as the grain's outward motion is slowed and it begins to move inward again, but is completed suddenly once w again falls below $10\,\text{km s}^{-1}$, in what we term *snap back*. The net result is that the grain has returned to exactly the same phase track that it started in on, and so repeats the cycle indefinitely.

The right panels of Figure 12 show the case where the stream velocity is doubled to $v_\infty = 80\,\text{km s}^{-1}$, but all other parameters remain the same. At this velocity, the equilibrium drift is stable and so the grain can achieve a stagnant drift solution, where it is stationary with respect to the star. The trajectory during the first approach is similar to the previous case, except that the overshoot of the rip point is greater, so that $R_{\text{min}} \approx 0.65R_\dagger$ in this case. This is a consequence of the fact that the rip point is closer to the drag-free turnaround radius ($R_\dagger/R_{**}$ is larger than in the lower velocity case), so that the grain inertia is relatively more important. A second consequence of this is that the speed of the initial expulsion is not so large, being only a little higher than the inflow velocity. The qualitative difference between the two cases emerges after the first recoupling: instead of the snap back and endless limit cycle, the grain oscillates about the stagnant drift radius with ever decreasing amplitude, so that after a few oscillation periods it has come to almost a complete rest.

Figure 13. Bow radius as a function of stream density for a stream of initial velocity $80\,\mathrm{km\,s^{-1}}$, which interacts with a $10\,\mathrm{M_\odot}$ main-sequence B star. This corresponds to a vertical slice through the left panel of Fig. 11. At low densities, the hydrodynamic bow shock (blue line) is larger than the drag-free turnaround radius for small carbon grains, meaning that a grain's inertia carries it into the bow shock along with the gas, even though the gas–grain coupling is not particularly strong. At densities above about $0.05\,\mathrm{cm^{-3}}$, however, this is no longer true and a separate dust wave forms outside of the hydrodynamic bow shock, which is now dust-free (green dashed line). The grains in the dust wave will occupy a range of radii (pale orange shading) between $R_{\min}$ (solid orange line) and $R_\ddagger$, the stagnant drift radius. At densities above about $1000\,\mathrm{cm^{-3}}$, the gas stream starts to feel the effect of passing through the dust wave, and above $3 \times 10^4\,\mathrm{cm^{-3}}$, the dust wave and bow shock merge to form a radiative bow wave (red line), which becomes an optically thick radiative bow shock (purple line) above $10^6\,\mathrm{cm^{-3}}$.

4.5 Back reaction on the gas flow

So far we have ignored the effect of the drag force on the gas stream itself, but it is clear that this must become important as τ_* approaches $\tau_{*,\max}$, since that is the point where the dust wave transitions to a bow wave, in which the dust and gas are perfectly coupled. A full treatment of this problem would require solving the hydrodynamic equations simultaneously with the equations of motion of the dust grains, which is beyond the scope of this paper. Instead, we outline a heuristic approach that qualitatively captures the physics involved.

The maximum drag force experienced by a grain is at the rip point. Since the grain follows a zero-net-force phase track up until that point, this can be written with the help of equations (1, 2) as

$$f_{\mathrm{drag}}(R_\dagger) = f_{\mathrm{rad}}(R_\dagger) = \frac{m_{\mathrm{d}} v_\infty^2 R_{**}}{2 R_\dagger^2} \qquad (25)$$

The timescale of the flow can be characterized by the crossing time $R_\dagger/v_\infty$, but the residence time of the grain at the bow apex will be several times larger than this (see previous section). On the other hand, the average drag force during this residence will be several times smaller than $f_{\mathrm{drag}}(R_\dagger)$ if $R_\ddagger > R_\dagger$, which is typically the case. We therefore parameterize our ignorance via a dimensionless factor, α, which we expect to be of order unity, and write the total impulse imparted to the grain by drag as

$$J_{\mathrm{drag}} \equiv \int f_{\mathrm{drag}}\, dt \approx \alpha f_{\mathrm{drag}}(R_\dagger) \frac{R_\dagger}{v_\infty} = \tfrac{1}{2}\alpha\, m_{\mathrm{d}} v_\infty \frac{R_{**}}{R_\dagger} . \qquad (26)$$

By Newton's Third Law, an equal and opposite impulse is

imparted to the gas, which will act to decelerate the gas stream as it decouples from the grains. Realistically, J_{drag} should be summed over the grain size distribution, but for simplicity we assume that all grains are identical, so that the mass of gas that accompanies each grain is given by

$$m_{\mathrm{gas}} = \frac{m_{\mathrm{d}}}{Z_{\mathrm{d}}} = m_{\mathrm{d}}\, \frac{\kappa_{\mathrm{d}}}{\kappa} . \qquad (27)$$

If the gas remains supersonic after decoupling, then thermal pressure can be ignored and the gas will suffer a change in momentum equal to J_{drag}, so that its velocity is reduced by $\Delta v = J_{\mathrm{drag}}/m_{\mathrm{gas}}$, which by equations (20, 22, 24, 26, 27) is

$$\Delta v = \tfrac{1}{2}\alpha \frac{\tau_*}{\tau_{*,\max}} v_\infty . \qquad (28)$$

This deceleration reduces the gas stream's ram pressure before it interacts with the central star's stellar wind. The radius of the dust-free bow shock formed by this interaction is therefore increased by a factor $(1 - \Delta v/v_\infty)^{-1}$ with respect to the case calculated in § **??**, yielding

$$R_{\mathrm{dfbs}} \approx \frac{\eta_{\mathrm{w}}^{1/2} R_*}{1 - \tfrac{1}{2}\alpha \tau_*/\tau_{*,\max}} . \qquad (29)$$

An example is illustrated in Figure 13, where the dust-free bow shock radius is shown by the green dashed line as a function of stream density, n. This is calculated for fixed stream velocity and grain and star properties, so that $\tau_* \propto n^{1/2}$ (eq. [**??**]). In order for R_{dfbs} to match the dust-wave and bow-wave radii at the point where they cross at $\tau_* = \tau_{*,\max}$, we find $\alpha \approx 1.5$ is required. It can be seen that the gas deceleration is negligible over most of the density range for which a separate dust wave arises. Only for $n > 10^3\,\mathrm{cm^{-3}}$ does R_{dfbs} begin to curve up from the general $n^{-1/2}$ trend, becoming essentially flat at a value $R_{\mathrm{dfbs}} \approx (\kappa/\kappa_{\mathrm{d}}) R_{**}$ until full-coupling is established at $n > 3 \times 10^4\,\mathrm{cm^{-3}}$. Note, however, that the treatment described here is very approximate: it does not take into account the shock that will form once J_{drag} reaches an appreciable fraction of $m_{\mathrm{gas}} v_\infty$ and, additionally, it includes a factor, α, whose value has not been rigorously justified. More detailed modeling is required to fully understand the bow behavior in this transition regime.

5 MAGNETIC COUPLING OF GRAINS

It remains to calculate in detail the effects on grain dynamics of the plasma's magnetic field, in order to justify the approach taken in § 2.3 and extend those results to include the effects of gas–grain collisions as in § 4. The Lorentz force on charged grains due to a magnetic field is

$$\boldsymbol{f}_{\mathrm{B}} = \frac{z_{\mathrm{d}} e}{c}\, \boldsymbol{w} \times \boldsymbol{B} . \qquad (30)$$

The direction of the force is perpendicular both to the magnetic field, $\boldsymbol{B}$, and to the relative velocity, $\boldsymbol{w}$, of the grain with respect to the plasma. If $\boldsymbol{w}$ and $\boldsymbol{B}$ (as seen by the grain) are changing slowly, compared with the gyrofrequency, $\omega_{\mathrm{B}} = z_{\mathrm{d}} e B/m_{\mathrm{d}} c$, then the grain motion perpendicular to $\boldsymbol{B}$ is constrained to be a circle of radius equal to the Larmor radius:

$$r_{\mathrm{B}} = \frac{m_{\mathrm{d}} c w_\perp}{|z_{\mathrm{d}}| e B} , \qquad (31)$$

where $B = |\boldsymbol{B}|$ and $w_\perp$ is the perpendicular component of $\boldsymbol{w}$. The component of $\boldsymbol{w}$ parallel to $\boldsymbol{B}$ is unaffected by $\boldsymbol{f}_{\mathrm{B}}$, so the resultant trajectory is helical.

The relative importance of the magnetic field can be characterized by the ratio of the Larmor radius to the minimum radius, $R_{\min}$, reached by the grain in the dust wave (see § 4.4), where $R_{\min} \approx R_\dagger$ for drag-confined dust waves (DDW), or $R_{\min} \approx R_{**}$ for inertia-confined dust waves (IDW). We write the field strength in terms of the Alfvén speed,

$$v_A = \frac{B}{(4\pi\rho_{\text{gas}})^{1/2}} = 1.9\,\frac{B}{\mu\text{G}}n^{-1/2}\,\text{km s}^{-1}\,, \qquad (32)$$

and the grain charge $z_d e$ in terms of the potential ϕ (eq. [14]) to obtain

$$\text{DDW:}\quad \frac{r_B}{R_{\min}} = \frac{r_B}{R_\dagger} = 0.0140\,a_{\mu m}^2\,\frac{w_\perp}{v_A}\left(\frac{\Xi_\dagger}{L_4 T_4}\right)^{1/2}\frac{\rho_d}{\phi_\dagger} \qquad (33)$$

and

$$\text{IDW:}\quad \frac{r_B}{R_{\min}} = \frac{r_B}{R_{**}} = 0.0544\,a_{\mu m}^3\,\frac{w_\perp}{v_A}\,\frac{v_{10}^2}{n^{1/2}}\,\frac{1}{L_4 T_4}\,\frac{\rho_d^2}{Q_p \phi_{**}}\,, \qquad (34)$$

where $a_{\mu m} = a/1\,\mu\text{m}$, ρ_d is the grain material density in g cm^{-3}, and we have made use of equations (2, 20), together with Paper I's equation (14).

If $r_B/R_{\min} \ll 1$, then the grains are so strongly coupled to the field that they can be treated in the guiding-center approximation, in which the trajectory is decomposed into a tight circular gyromotion around the field lines, plus a sliding of the guiding center along the field lines, which is governed by the radiation and drag forces (the slow $f \times B$ drift across the field lines is negligible in this case, see App. 2.3). In the opposite limit, $r_B/R_{\min} \gg 1$, magnetic coupling is so weak that the non-magnetic results of § 4 are scarcely modified. Assuming $w_\perp \sim v_\infty$ and adopting a threshold of $r_B/R_{\min} < 0.1$, equations (33, 34) can be transformed into conditions on the stream velocity (in km s^{-1}) where tight magnetic coupling will apply:

$$v_\infty < v_{\text{tight}} \approx \begin{cases} \text{drag-confined:} & 0.8\,a_{\mu m}^{-2}\,v_A\,L_4^{1/2} \\ \text{inertia-confined:} & 6\,a_{\mu m}^{-1}\,v_A^{1/3}\,n^{1/6}\,L_4^{1/3} \end{cases}, \qquad (35)$$

where we have substituted typical values of the minor parameters $\Xi_\dagger$, $\phi_\dagger$, ϕ_{**}, ρ_d, T_4.[11] It is apparent that v_{tight} is very sensitive to the grain size. For instance, taking a typical H II region value of $v_A = 2$ km s^{-1} (Arthur et al. 2011) and $L_4 = 0.63$ (Tab. **??**, B1.5 V star), then for the drag-confined case $v_{\text{tight}} \approx 30$ km s^{-1} for 0.2 µm grains but $v_{\text{tight}} \approx 3000$ km s^{-1} for 0.02 µm grains. Thus, for typical stream velocities of 20 km s^{-1} to 100 km s^{-1}, the small grains are always tightly coupled to the magnetic field, but the large grains are only loosely coupled for the faster streams.

5.1 Grain trajectories with tight magnetic coupling

We can now investigate how the results of the previous sections are modified by magnetic fields in the tight coupling limit. For simplicity, we assume a uniform field in the incoming stream, with field lines oriented at an angle θ_B to the velocity vector that defines the bow axis. We also assume a super-alfvénic stream, $v_\infty > v_A$, so that the radius, R_0, of the wind bow shock is unaffected by the magnetic field, and additionally assume $\tau_* \ll \tau_{*,\max}$, so that the back-reaction of the grain drag on the plasma is negligible (see previous section)

and B remains uniform in magnitude and direction in the dust wave region, outside of the bow shock.

In Appendix 2.3, we derive analytic and semi-analytic results in the limit of zero gas–grain drag, which is appropriate for inertia-confined dust waves. We find very different structures, depending on the orientation of the field. For a parallel field (Fig. 2), the apex of the dust wave occurs at the same point, R_{**}, as in the non-magnetic case, but the shape of the dust wave wings is more closed, being hemispherical rather than parabolic in shape. For a perpendicular field (Fig. 3), on the other hand, grains in the apex region are dragged very close to the star and no dust wave forms there. A dust wave can form in the wings, with impact parameter $> R_{**}$, which is roughly parabolic in shape, but more swept-back than in the non-magnetic case. Whether such a dust wave will exist in practice depends critically on the size and shape of the MHD wind-supported bow shock.

In Figures 14 and 15 we show example results for drag-confined dust waves, which are calculated by numerically integrating the grain's equation of motion, as described in Appendix A. Apart from the inclusion of the magnetic field, the model parameters are the same as used in Figure 12, with the exception that the stream density is increased to 10 cm^{-3}.[12] This time, we use quasi-parallel ($\theta_B = 10°$) and quasi-perpendicular ($\theta_B = 75°$) field orientations. The quasi-parallel field is most similar to the non-magnetic case, and the models shown in the two upper panels of Figure 14 closely mirror the cases shown in Figure 12, with a limit cycle behavior when $v_\infty = 40$ km s^{-1} and stagnant drift when $v_\infty = 80$ km s^{-1}.

The principle difference from the 1-D axial trajectories discussed in § 4.4 is that the small 10° misalignment of B from the incident stream direction causes a slow sideways migration, which puts a finite limit on the time a grain can reside in front of the star. This can be appreciated more clearly in Figure 15, which shows the grain position and velocity along a sample streamline with initial impact parameter $b = -0.4 R_\dagger$ for the two quasi-parallel models. In panel a, corresponding to $v_\infty = 40$ km s^{-1}, we see the same rip-and-snap-back cycle of de-coupling and re-coupling that was discussed previously, but only two periods of the cycle are completed before the grain's lateral migration takes it as far as $y \approx +R_\dagger$, at which point nothing can stop the gas stream from dragging it past the star and away. All told, the grain remains in the apex region for about $1/\sin\theta_B$ times longer than the crossing time, $R_\dagger/v_\infty$.

In panel b, corresponding to $v_\infty = 80$ km s^{-1}, the grain settles for a while around the stagnant drift radius, $R_\ddagger$, after the initial rip and turn around. Again, it slowly migrates sideways, and eventually recouples to the incident stream, but this time after reaching $y \approx +R_\ddagger$. The grain residence time in the apex region, measured in crossing times, is slightly longer than in panel a, but is of the same order. In both these cases, a second, exterior dense shell is formed in addition to the hemispherical one produced by the initial turn around inside $R_\dagger$. In the limit-cycle case, it forms at the snap-back point, while in the stagnant-drift case, it forms at $R_\ddagger$ and is significantly denser than the interior shell (upper right panel of Fig. 14).

The assumptions behind these models break down when the grain trajectory intersects the outer shock of the dust-free wind-supported bow shock. The increased gas density in the bow shock shell will reduce Ξ, which is likely to cause gas–grain recoupling in the case of drag-confined dust waves (see also discussion in the final

---

[11] The most significant systematic variation in v_{tight} from these suppressed parameters is due to grain composition, yielding slightly higher values for graphite than for silicate (± 0.15 dex).

[12] The reason for using a higher density is to decrease the amplitude of the radial oscillations of the trajectories, which allows the dust wave structure to be more clearly perceived in the figures.
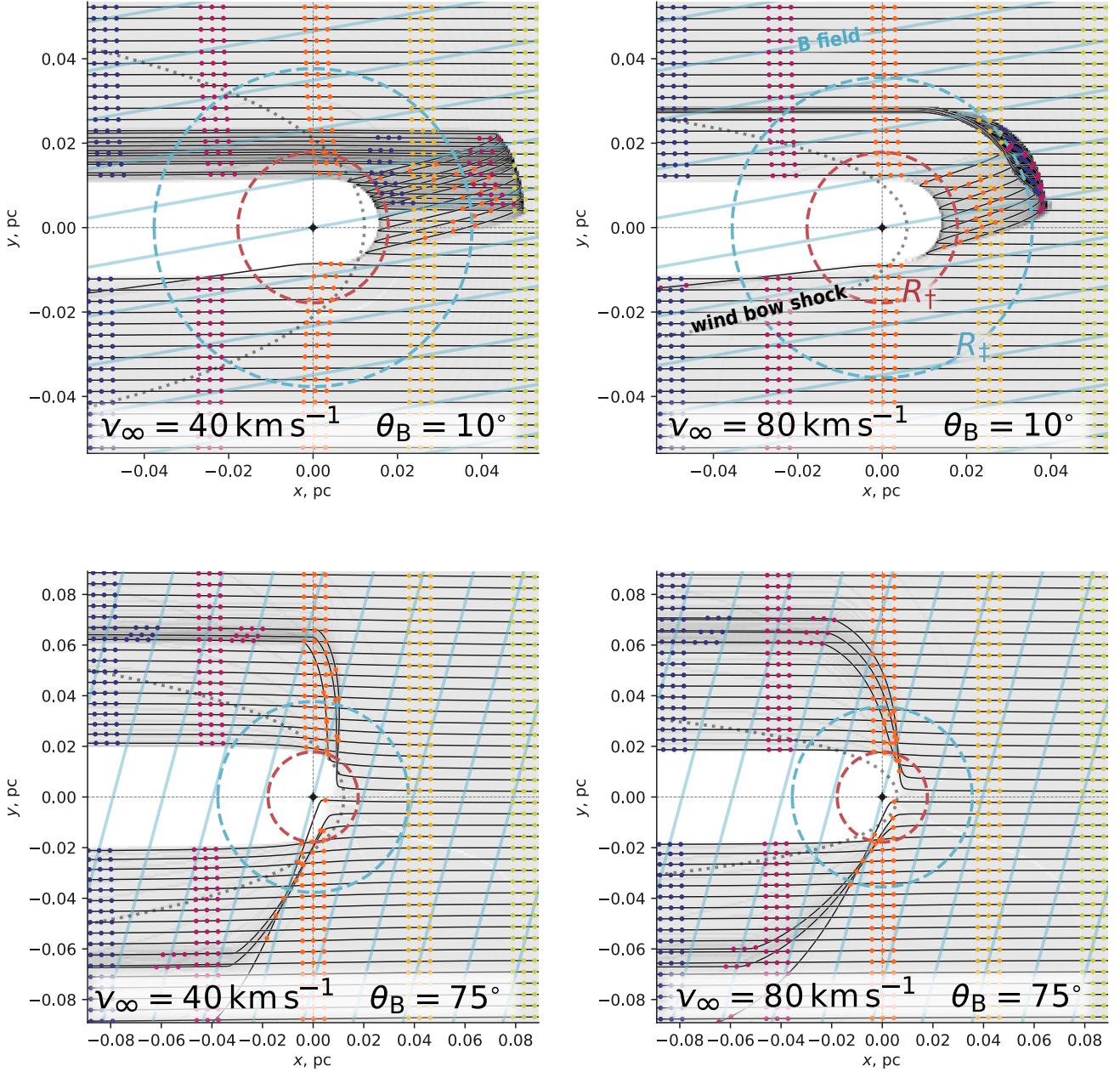
Figure 14. Drag-confined dust waves with tight magnetic coupling. Upper panels show a quasi-parallel field, $\theta_B = 10°$, while lower panels show a quasi-perpendicular field, $\theta_B = 75°$. Left panels show an incident stream velocity of $v_\infty = 40\,\mathrm{km\,s^{-1}}$, while right panels show $v_\infty = 80\,\mathrm{km\,s^{-1}}$. In all cases, the stream density is $n = 10\,\mathrm{cm^{-3}}$ and the calculations are performed for small graphite grains, $a = 0.02\,\mu\mathrm{m}$, and the $10\,\mathrm{M_\odot}$ main-sequence B star. Continuous black lines show grain trajectories, with triplets of colored symbols indicating the progress of individual cohorts, which entered from the right edge at a particular time. Continuous blue lines show the magnetic field, which flows from right to left along with the incident stream. The radius of the rip point, $R_\dagger$, and the stagnant drift point, $R_\ddagger$, are shown respectively by red and blue dashed lines. The approximate shape of the wind-supported bow shock is shown by the dotted gray line. The calculations are no longer valid after trajectories cross this surface.

paragraph of § 4.3). However, detailed modeling of this requires magnetohydrodynamical simulations, which are beyond the scope of this paper. In Figure 14 we show in gray dotted lines the Wilkinoid surface (Wilkin 1996), which is an approximation to the shape of the inner bow shock, see Paper I. It can be seen that the majority of dust streamlines do not cross this surface until well into the wings

of the bow, so that a separate exterior dust wave can exist for this quasi-parallel magnetic field orientation.

This is no longer the case for the quasi-perpendicular field orientation, as illustrated in the lower panels of Figure 14, where the behavior is similar to the perpendicular inertia-confined case studied in Appendix 2.3.2. Although the grains decouple from the gas inside
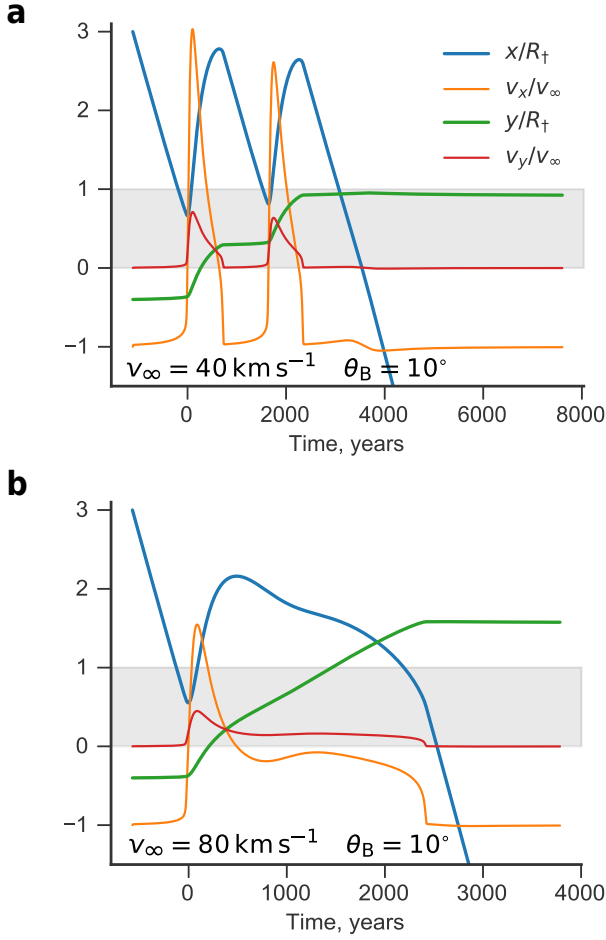
Figure 15. Sample grain trajectories for drag-confined dust waves with tight magnetic coupling and a quasi-parallel field orientation. These are the same models as in the upper row of Fig. 14. (a) Incident stream velocity of $v_\infty = 40 \, \text{km s}^{-1}$, showing quasi-limit-cycle behavior (0 to 4000 years). (b) Incident stream velocity of $v_\infty = 80 \, \text{km s}^{-1}$, showing quasi-stagnation behavior (500 to 2000 years). In both cases, the streamline with initial impact parameter $y = -0.4R_\dagger$ is shown.

the rip point, for small impact parameters the magnetic geometry does not allow the radiation field to expel them until they are much nearer to the star. Since the inner wind-supported bow shock radius is only a few times smaller than $R_\dagger$, it is possible that they will pass through the shock surface and re-couple before expulsion can occur. For the $40 \, \text{km s}^{-1}$ model (lower left panel), all of the streamlines with impact parameters $|b| < R_\dagger$ intersect the Wilkinoid surface before they are deflected, and so no separate dust wave would form in this case. For the $80 \, \text{km s}^{-1}$ model (lower left panel), some of the streamlines (mainly those with $b > 0$) do manage to avoid crossing the bow shock surface, so it is possible that a dust wave may still form, although it would only be on one side of the axis.

ACKNOWLEDGEMENTS

This work has made extensive use of Python language libraries from the SciPy (Jones et al. 2019) and AstroPy (Astropy Collaboration et al. 2013, 2018) projects.

REFERENCES

Abel N. P., Hoof P. A. M. v., Shaw G., Ferland G. J., Elwert T., 2008, ApJ, 686, 1125
Arthur S. J., Henney W. J., Mellema G., de Colle F., Vázquez-Semadeni E., 2011, MNRAS, 414, 1747
Astropy Collaboration et al., 2013, A&A, 558, A33
Astropy Collaboration et al., 2018, preprint, (arXiv:1801.02634)
Baines M. J., Williams I. P., Asebiomo A. S., 1965, MNRAS, 130, 63
Baldwin J. A., Ferland G. J., Martin P. G., Corbin M. R., Cota S. A., Peterson B. M., Slettebak A., 1991, ApJ, 374, 580
Bohren C. F., Huffman D., 1983, Absorption and scattering of light by small particles. Wiley-VCH
Chandrasekhar I. S., 1941, ApJ, 93, 285
Draine B. T., Salpeter E. E., 1979, ApJ, 231, 77
Ferland G. J., et al., 2013, Rev. Mex. Astron. Astrofis., 49, 137
Ferland G. J., et al., 2017, Rev. Mex. Astron. Astrofis., 53, 385
Hindmarsh A. C., 1983, IMACS Transactions on Scientific Computation, 1, 55
Jones E., Oliphant T., Peterson P., et al., 2001–2019, SciPy: Open source scientific tools for Python, http://www.scipy.org/
Landau L., Lifshitz E., 1976, Mechanics, 3rd edn. Course of Theoretical Physics S Vol. 1, Butterworth-Heinemann
Lanz T., Hubeny I., 2003, ApJS, 146, 417
Lanz T., Hubeny I., 2007, ApJS, 169, 83
Spitzer L., 1978, Physical processes in the interstellar medium. New York: Wiley-Interscience
Tarango-Yong J. A., Henney W. J., 2018, MNRAS, 477, 2431
Weidenschilling S. J., 1977, MNRAS, 180, 57
Weingartner J. C., Draine B. T., 2001a, ApJS, 134, 263
Weingartner J. C., Draine B. T., 2001b, ApJ, 548, 296
Weingartner J. C., Draine B. T., Barr D. K., 2006, ApJ, 645, 1188
Wilkin F. P., 1996, ApJ, 459, L31
van Hoof P. A. M., Weingartner J. C., Martin P. G., Volk K., Ferland G. J., 2004, MNRAS, 350, 1330

APPENDIX A: EQUATION OF MOTION FOR GRAINS WITH RADIATION, GAS DRAG, AND MAGNETIC FIELD

Following Draine & Salpeter (1979), the drag force on a grain that is moving at relative velocity $\boldsymbol{w} = \boldsymbol{v}_\text{d} - \boldsymbol{v}_\text{gas}$ through a partially ionized gas can be written as a sum over each collider species, k, with mass m_k, abundance relative to hydrogen α_k and charge z_k. If the relative speed, $w = |\boldsymbol{w}|$, is normalized to the thermal speed of each species:

$$s_k = \left(m_k w^2 / 2kT \right)^{1/2} , \tag{A1}$$

then the magnitude of the force is

$$f_\text{drag} = f_* \sum_k \alpha_k \left[G_0(s_k) + z_k^2 \phi^2 \ln(\Lambda/z_k) G_2(s_k) \right], \tag{A2}$$

where f_* is a characteristic thermal force on the grain (see eq. [15]). The dimensionless functions of normalized speed $G_0(s)$ and $G_2(s)$ are given by

$$G_0(s) = \left(s^2 + 1 - \frac{1}{4s^2} \right) \text{erf}(s) + \left(s + \frac{1}{2s} \right) \frac{e^{-s^2}}{\sqrt{\pi}} \tag{A3}$$

$$G_2(s) = \frac{\text{erf}(s)}{s^2} - \frac{2e^{-s^2}}{s\sqrt{\pi}} . \tag{A4}$$

The G_0 term is due to inelastic solid-body collisions in the Epstein limit, and is derived in § 4 of Baines et al. (1965). The G_2 term is due to electrostatic Coulomb interactions, with ϕ being the grain potential in thermal units (eq. [14]) and Λ the plasma parameter. It was first derived in the different context of dynamical friction in stellar systems by Chandrasekhar (1941). Figures 8–10 show example applications to gas–grain drag in a photoionized region.

The grain trajectories presented in § 4.4 and 5.1 are calculated by numerically solving the grain equation of motion:

$$m_\mathrm{d} \frac{d^2 \boldsymbol{r}}{dt^2} = \boldsymbol{f} \; . \tag{A5}$$

The total force $\boldsymbol{f}$ is the sum of radiation, drag, and Lorentz terms:

$$\boldsymbol{f} = \frac{\sigma_\mathrm{d} Q_\mathrm{p} L}{4\pi R^2 c} \hat{\boldsymbol{r}} - f_\mathrm{drag} \hat{\boldsymbol{w}} + \frac{z_\mathrm{d} e}{c} \boldsymbol{w} \times \boldsymbol{B} \; , \tag{A6}$$

with f_drag given by equation (A2) and where $\hat{\boldsymbol{r}}$ is the unit vector in the radial direction and $\hat{\boldsymbol{w}} = \boldsymbol{w}/w$ is the unit vector along the direction of gas–grain relative motion. In the strong magnetic coupling limit (see § 5.1 and 2.3), the Lorentz term is not included explicitly, but instead the equation of motion is solved for the guiding center by replacing $\boldsymbol{f}$ by its projection along the magnetic field:

$$\widetilde{\boldsymbol{f}} = (\boldsymbol{f} \cdot \hat{\boldsymbol{b}}) \hat{\boldsymbol{b}} \; , \tag{A7}$$

where $\hat{\boldsymbol{b}} = \boldsymbol{B}/B$.

If distances are measured in units of the radiative turnaround radius, R_{**} (eq. [2]), and times in units of R_{**}/v_∞, then the grain acceleration $\boldsymbol{a}_\mathrm{d} = \boldsymbol{f}/m_\mathrm{d}$ in the non-magnetic case can be written in non-dimensional form as

$$\frac{\boldsymbol{a}_\mathrm{d}}{a_{**}} = \frac{R_{**}^2}{2R^2} \hat{\boldsymbol{r}} - C_\mathrm{drag} \frac{f_\mathrm{drag}}{f_*} \hat{\boldsymbol{w}} \tag{A8}$$

where $a_{**} = v_\infty^2/R_{**}$ is a characteristic acceleration scale and the dimensionless drag constant is

$$C_\mathrm{drag} = \frac{4}{Q_\mathrm{p}} \left(\frac{c_\mathrm{s} \tau_* \kappa_\mathrm{d}}{v_\infty \kappa} \right)^2 \; . \tag{A9}$$

A collection of python programs that implement the equations of this appendix is available at https://github.com/div-B-equals-0/dust-trajectories, including programs to generate all the grain trajectory figures of this paper plus additional figures and movies. The integration of equation (A8) is carried out using the python library function `scipy.integrate.odeint`, which wraps the Fortran ODEPACK library (Hindmarsh 1983; Jones et al. 2019).

This paper has been typeset from a TEX/LATEX file prepared by the author.